Wind and Structures, *Vol. 20, No. 2 (2015) 143-168*
DOI: http://dx.doi.org/10.12989/was.2015.20.2.143

Dynamics of high-speed train in crosswinds based on an air-train-track interaction model

Wanming Zhai*[1], Jizhong Yang[2], Zhen Li[1] and Haiyan Han[3]

[1]*Train and Track Research Institute, State Key Laboratory of Traction Power, Southwest Jiaotong University, Chengdu 610031, P.R. China*
[2]*China Railway Eryuan Engineering Group Co. Ltd., No. 3 Tongjin Road, Chengdu 610031, P.R. China*
[3]*Beijing Urban Construction Design and Development Group Co. Ltd, Beijing, P.R. China*

(Received November 20, 2014, Revised December 23, 2014, Accepted January 5, 2015)

Abstract. A numerical model for analyzing air–train–track interaction is proposed to investigate the dynamic behavior of a high-speed train running on a track in crosswinds. The model is composed of a train–track interaction model and a train–air interaction model. The train–track interaction model is built on the basis of the vehicle–track coupled dynamics theory. The train–air interaction model is developed based on the train aerodynamics, in which the Arbitrary Lagrangian–Eulerian (ALE) method is employed to deal with the dynamic boundary between the train and the air. Based on the air–train–track model, characteristics of flow structure around a high-speed train are described and the dynamic behavior of the high-speed train running on track in crosswinds is investigated. Results show that the dynamic indices of the head car are larger than those of other cars in crosswinds. From the viewpoint of dynamic safety evaluation, the running safety of the train in crosswinds is basically controlled by the head car. Compared with the generally used assessment indices of running safety such as the derailment coefficient and the wheel-load reduction ratio, the overturning coefficient will overestimate the running safety of a train on a track under crosswind condition. It is suggested to use the wheel-load reduction ratio and the lateral wheel–rail force as the dominant safety assessment indices when high-speed trains run in crosswinds.

Keywords: high-speed train; dynamic safety; crosswind; aerodynamics; vehicle–track coupled dynamics; Arbitrary Lagrangian–Eulerian method

1. Introduction

Generally, the running safety of a train on a track in crosswinds decreases with the increase of wind speed. Fig. 1 shows a train derailment caused by a strong sandstorm in Xinjiang, China, in February 2007. Eleven cars of the train running between Urumqi and Aksu were overturned by the strong wind. At least four passengers were killed and more than 30 injured in this accident. It is convinced when the train runs at high speeds in crosswinds the problem of operational safety becomes even more serious. Motivated by the desire to ensure the running safety and improve the ride quality of high-speed trains in crosswinds, a lot of studies have been carried out on railway vehicle dynamics, train–track coupled dynamics and train aerodynamics, respectively, through

*Corresponding author, Professor, E-mail: wmzhai@swjtu.edu.cn

http://www.techno-press.org/?journal=was&subpage=8 ISSN: 1226-6116 (Print), 1598-6225 (Online)

running tests, numerical simulations, and wind tunnel experiments. However, appreciable differences between the calculation results and the actual ones exist due to the fact that there are still some challenging issues and uncertainties remaining in computational fluid dynamics (CFD) technique (Xu 2013).

The running safety of train is a focus in railway vehicle dynamics. In the classical theory of vehicle dynamics (Garg and Dukkipati 1984), the train running safety is always studied in the absence of side wind. Some safety indices were proposed to evaluate the running safety, such as the derailment coefficient, the overturning coefficient, the wheel-load reduction ratio, the wheel–rail lateral force, etc. Classical vehicle dynamics theory usually takes the railway vehicle system itself as the analysis object without consideration of the dynamic behavior of the track system on which the vehicle is supported, i.e., the track structure is assumed to be a rigid base. With the increase in train speed, effects of dynamic interaction between the vehicle and the track obviously intensify. Thus, the character of track structure will affect the running safety of the train and should be taken into account in the analysis model. Several models have been developed to consider the vertical coupling effect of the vehicle and the track (Zhai and Sun 1994, Dahlberg 1995, Sun and Dhanasekar 2002). Relative few studies can be found on the lateral interaction between the vehicle and the track (Zhai *et al*. 1996, Zhai and Wang 2006). Zhai *et al*. (2009) has set up a framework for analyzing the overall three-dimensional vehicle–track coupled system dynamics, which can be used to investigate the lateral stability and the running safety of a vehicle on an elastic track structure, instead of on a rigid track base (Zhai and Wang, 2010).

When a train is cruising in the crosswind, the wind loads acting on the high-speed train will impair the running safety. Even worse, the running train may be overturned when the wind is strong enough. In order to evaluate the running safety of train in crosswinds, the aerodynamic loads on train needs to be achieved at first. In an attempt to estimate aerodynamic forces on a moving vehicle, some hypotheses have been set up and a foundation for investigating wind effects on a moving vehicle has been laid down (Balzer 1977, Chiu 1991, Chiu 1995). The wind acting on a moving vehicle has been further investigated (Cooper 1984, Baker 1991a,b), in which the aerodynamic loads are divided into two parts: steady aerodynamic forces and unsteady aerodynamic forces. Khier (2000) has carried out numerical investigations of different flow structures by the three-dimensional Reynolds-averaged Navier–Stokes (RANS) equations, combined with the k-ε turbulence model, which were solved on a multi-block structured grid using the finite volume technique. Diedrichs (2003) has compared different numerical schemes and turbulence models for Deutsche Bahn AG's reference train ICE 2, which are applied to calculate the aerodynamic loads. In his work, a set of independent aerodynamic coefficients are obtained for three models using the same train composed of two and a half cars. Recently, Rezvani and Mohebbi (2014) employed the three-dimensional RANS equations to investigate the unsteady aerodynamic performance of crosswind around the ATM train under different yawing conditions. Li *et al*. (2014) carried on wind tunnel test to obtain the aerodynamic forces and moments acting on the moving vehicle model on the bridge deck in crosswinds. Herbsta *et al*. (2014) introduced some aerodynamic prediction tools for high-speed trains, especially an efficient technique to analyse complex wake flows with regard to slipstream.

The vehicle stability under crosswind is usually studied in the absence of track irregularities by the principle of static equilibrium, in which the overturning coefficient or the wheel-load reduction ratio is commonly used to evaluate the safety (Diedrichs 2007). However, the most deserving attentive aspect is the dynamic performance of a train in crosswinds, because it is much poorer than the static case. The dynamic performance of a train has relations not only with aerodynamic

effect, but also with vehicle system itself, coupling devices between two vehicles, wheel–rail contact relationship, track and infrastructure system, etc. To have a full understanding of this phenomenon, these factors should be taken into consideration synthetically, especially for high-speed trains. Therefore, it is worth doing a deep investigation on dynamic interaction between the high-speed train and its surrounding air as well as the track system.

With the development of vehicle–track coupled dynamics and train aerodynamics, it is possible to combine them to evaluate the dynamic safety of the train running on the track in crosswind. Generally, the calculated wind loads are input to the vehicle system as external loads that are assumed to be immune to the vehicle vibration (Xu and Ding 2006, Xia *et al*. 2008). However, the vibration of car body could alter the boundary condition between the train and the air and consequently may change the wind loads. Compared with the scale of the train and the surrounding flow field, the train lateral movement is too small to have a great influence on the whole flow field. Nevertheless, the train vibration can strongly affect the flow turbulence nearby the train, which could in turn affect the aerodynamic forces on the train, especially when the train travels in tunnels. In 1986, the lateral vibration of car body was aggravated when the train speed was enhanced in the tunnels of Japanese Tokaido–Sanyo high-speed railway. After a long time survey, it is found that the excessive lateral vibration of the car body in tunnel is caused by the train–air interaction (Suzuki *et al*. 2001). Li *et al*. (2005) developed an analytical model to study the dynamics of wind–vehicle–bridge systems by regarding the wind, rail vehicles and bridge as a coupled vibration system. Recently, Li *et al*. (2013) carried on a dynamic analysis on the interaction between two trains based on a wind–vehicle–bridge model. Xia *et al*. (2008) employed a wind–train–bridge system model to explore the dynamic response of the bridge, the running safety and stability of the train under the action of wind.

This paper intends to systematically investigate the running safety of a high-speed train on an elastic track in crosswinds from the viewpoint of the air–train–track interaction system. A three-dimensional model of a train running on a ballasted track will be described based on the vehicle-track coupled dynamics theory. An approach based on the Arbitrary Lagrangian–Eulerian (ALE) scheme is presented to investigate the dynamic interaction between the train and the air in crosswinds. The proposed air–train–track interaction model is finally applied to solve the dynamics problem of a high-speed train running on a straight embankment track substructure in crosswinds. The air flow structure around the high-speed train is simulated. The running safety of the high speed train in crosswinds is investigated, in which different assessment indices for determining the critical wind speed are compared.

Fig. 1 Train overturning caused by strong wind in Xinjiang, China

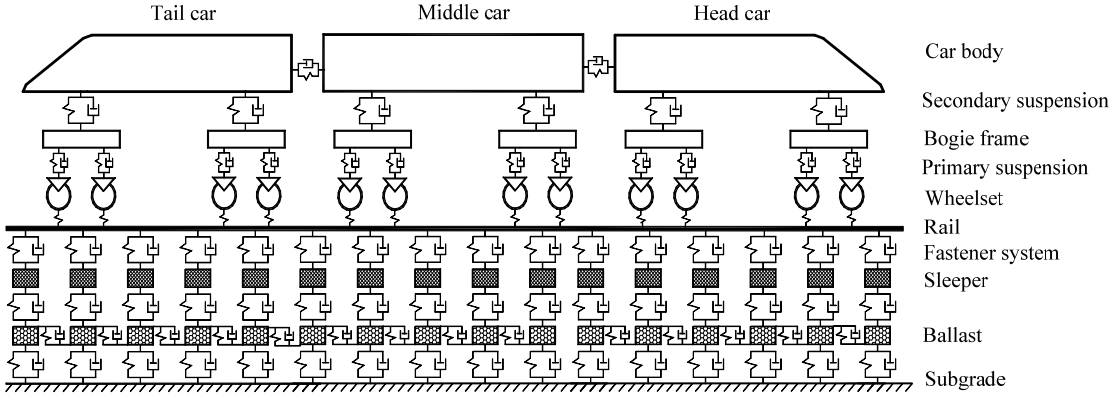

Fig. 2 Three-dimensional train–track interaction model (elevation)

2. Air–train–track interaction model

In this paper, an air–train–track interaction model is established to study the dynamic performance of a high-speed train on a track in crosswinds. This model is composed of a train–track interaction model and a train–air interaction model in which the ALE method is utilized to deal with the dynamic boundary between the train and the air.

2.1 Train–track interaction model

The train–track interaction model is established based on the theory of vehicle–track coupled dynamics (Zhai *et al*. 2009). The train–track coupled system is divided into two subsystems: the train subsystem and the track subsystem. For each subsystem, the corresponding dynamic model is established, and then the two subsystems are coupled through the wheel–rail contacts.

A high-speed train model which consists of three 4-axle car sub-models, the minimum train set, is illustrated in Figs. 2 and 3. The meaning of notations used in the figures can be found in the work by Zhai *et al*. (2009). The main difference between the present model and the model used in the published paper (Zhai *et al*. 2009) is that multiple cars are considered instead of one car, in which the middle car sub-model is linked with the other two by spring-damper elements. In the car sub-model, the bogie frames are linked with the wheelsets through the primary suspensions and linked with the car body through the secondary suspensions. Three-dimensional spring-damper elements are used to represent the primary and the secondary suspensions. Yaw dampers and the lateral stop-blocks are considered in the secondary suspensions. The car model has seven rigid bodies including one car body, two bogie frames and four wheelsets, and each rigid body has five degrees of freedom (DOFs) without consideration of the one relating to the longitudinal vibration, thus, the number of total DOFs of each car sub-model is 35.

The track sub-model shown in Figs. 2 and 3 consists of the rails, the rail pads, the sleepers, the ballast and the subgrade. Two parallel rails of the track are modeled as continuous beams supported by a discrete–elastic foundation of three layers with sleepers and ballasts included. Vertical and lateral springs and dampers are considered to represent the dynamic properties in the

fastener system. Similarly, springs and dampers are used between the sleeper and the ballast to represent the elasticity and damping property in both the vertical and lateral directions.

The train subsystem and the track subsystem are coupled through the wheel–rail coupling relationship by the dynamic forces between the wheels and the rails. In the model, the wheel–rail normal contact forces $N(t)$ are calculated by the nonlinear Hertzian elastic contact theory according to the elastic compression deformation of wheels and rails at contact points in the normal directions

$$N(t)=\left[\frac{1}{\mathrm{G}}\delta Z_{\mathrm{N}}(t)\right]^{3/2} \tag{1}$$

where G is the wheel–rail contact coefficient and $\delta Z_{\mathrm{N}}(t)$ is elastic compression deformation.

The tangential wheel–rail creep forces are first calculated by the Kalker's linear creepage theory

$$\begin{cases} F_x=-f_{11}\xi_x \\ F_y=-f_{22}\xi_y-f_{23}\xi_{sp} \\ M_z=f_{23}\xi_y-f_{33}\xi_{sp} \end{cases} \tag{2}$$

where f_{ij} are the creep coefficients ; ξ_x, ξ_y and ξ_{sp} are longitudinal, lateral and spin creepages, respectively. And then, the wheel–rail creep forces are modified by Johnson–Vermeulen's nonlinear creepage model (Garg and Dukkipati 1984)

$$\begin{cases} F_x'=\varepsilon\cdot F_x \\ F_y'=\varepsilon\cdot F_y \\ M_z'=\varepsilon\cdot M_z \end{cases} \tag{3}$$

where ε is modified factor

$$\varepsilon=F_R'/F_R \tag{4}$$

in which

$$F_R=\sqrt{F_x^{\,2}+F_y^{\,2}} \tag{5}$$

$$F_R'=\begin{cases} fN\left[\dfrac{F_R}{fN}-\dfrac{1}{3}\left(\dfrac{F_R}{fN}\right)^2+\dfrac{1}{27}\left(\dfrac{F_R}{fN}\right)^3\right] & \text{when } F_R\le 3fN \\ fN & \text{when } F_R>3fN \end{cases} \tag{6}$$

where f is the friction coefficient between the wheel and the rail.

According to Newton's law and the law of momentum, the equations of motion of the train–track coupled system can be derived and expressed as

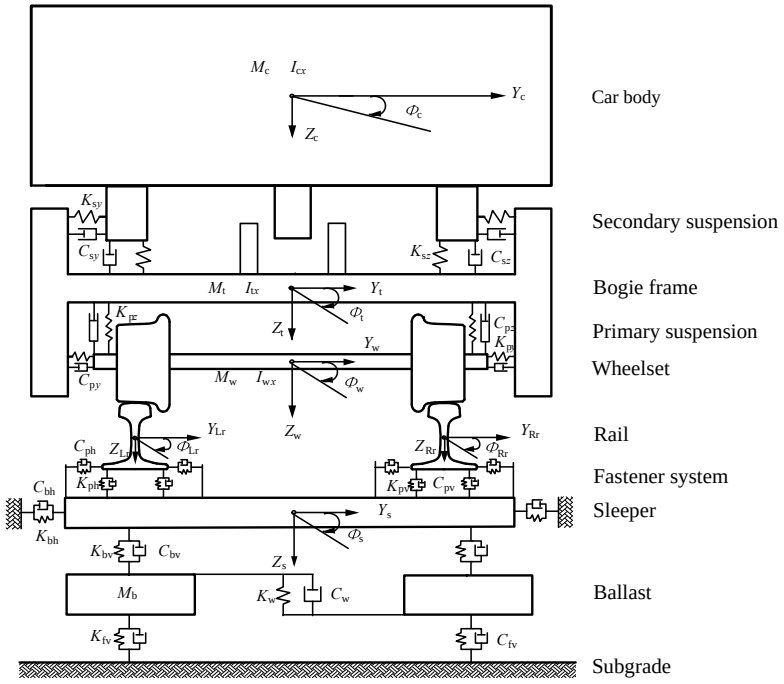

Fig. 3 Three-dimensional train–track interaction model (end view)

$$\mathbf{M}\ddot{\mathbf{X}} + \mathbf{C}\dot{\mathbf{X}} + \mathbf{K}\mathbf{X} = \mathbf{P} \tag{7}$$

where **M**, **C** and **K** are the mass, damping and stiffness matrices, respectively; **X** is the displacement vector; $\dot{\mathbf{X}}$ is the velocity vector; $\ddot{\mathbf{X}}$ is the acceleration vector; and **P** is the load vector including the wind-induced loads. More detailed differential equations of the train subsystem and the track subsystem can be found in references (Zhai *et al*. 1996, Zhai *et al*. 2009).

2.2 Train–air interaction model

In the traditional study of train aerodynamics, the boundary between the train and the air is assumed to be all through stationary. In fact, when the train is running in the strong crosswinds, the boundary between the train and the air is dynamic due to the vibration of vehicles. Once the boundary changes, the flow structure around the running train will alter and thereby the aerodynamic forces acting on the train will change. On the basis of the traditional train aerodynamics, the ALE method is employed to deal with the dynamic boundary between the train and the air, so as to realize the numerical simulation of train–air dynamic interaction.

2.2.1 Train aerodynamics

Different turbulent models are adopted to carry out simulation of vehicles running under crosswind conditions for different purposes. In numerical calculation of turbulence flow around train, the RANS k-ε model has been widely used (Khier *et al*. 2000, Khier *et al*. 2002, Li and Tian

2012, Cheli *et al*. 2010, Diedrichs 2010). The ability of standard k-ε model has been judged against other models by Khier (1997). Through comparisons, Khier concluded that the standard k-ε model can be employed with confidence to predict the global flow structure and for sensitivity analysis purposes (Khier *et al*. 2000). Sterling *et al*. (2010) has compared the results of the full-scale measurements, the wind tunnel test and the computational fluid dynamics (CFD) simulations implemented by the software package CFX using the unsteady RANS k-ε model. He found that the pressure distribution over selected sections of the lorry between the tunnel test and CFD is different. However, if these pressure distributions are area averaged (in order to calculate the mean force/moment coefficients), then in general, the disagreements between the simulations can be reduced. It is shown that the rolling moment coefficients obtained from the full-scale measurement and the CFD simulation agree consistently across a wide range of yaw angles. A good agreement of side force coefficients between the wind tunnel and the CFD data is also found. Based on the conclusions above, the standard RANS k-ε model is adopted in this paper to compute the train aerodynamic forces, which are then used as the wind loads in investigation of the running safety of high-speed train in crosswind.

For the flow case under consideration, the time averaged variant of Navier-Stokes equations combined with the eddy viscosity hypothesis represent the most accurate method among those feasible ones. The basic governing equations of the air are given in Eulerian forms as follows

The conservation equation for continuity

$$\frac{\partial \rho}{\partial t}+\frac{\partial \rho v_j}{\partial x_j}=0 \tag{8}$$

The conservation equation for momentum

$$\frac{\partial \rho v_i}{\partial t}+\frac{\partial}{\partial x_j}(\rho v_i v_j-p_{ij})=\rho g_i \tag{9}$$

The conservation equation for energy

$$\frac{\partial \rho E}{\partial t}+\frac{\partial}{\partial x_j}(\rho v_j E-p_{ij}v_i-\mu B\frac{\partial I}{\partial x_j})=\rho v_j g_j \tag{10}$$

In Eqs. (8)-(10), ρ is the air density; v_i is the air velocity vector; the stress tensor p_{ij} including both the scalar pressure and the viscous stress can be written as $p_{ij}=-p\delta_{ij}+0.5\lambda e_{kk}\delta_{ij}+\mu e_{ij}$, where p, the scalar pressure, is a prescribed function of the air density ρ and the specific internal energy I; δ_{ij} is the Kronecker delta; the viscosity coefficients of air, λ and μ, have, for simplicity, been chosen as constants. In addition, g_i represents gravity acceleration. The total specific energy E is defined like that $E=0.5v_i^2+I$. The heat conduction term, namely the temperature, has been altered by introducing the coefficient B.

The conservation equation for turbulent kinetic energy k is expressed as

$$\frac{\partial \rho k}{\partial t}+\frac{\partial}{\partial x_j}(\rho v_j k-\mu_{eff}\frac{\partial k}{\partial x_j})=G_k \tag{11}$$

The conservation equation for dissipation rate ε is described as

$$\frac{\partial \rho \varepsilon}{\partial t} + \frac{\partial}{\partial x_j}(\rho v_j \varepsilon - \mu_{eff} \frac{\partial \varepsilon}{\partial x_j}) = G_\varepsilon \tag{12}$$

where

$$\begin{cases} G_k = \mu_t \dfrac{\partial v_i}{\partial x_j} e_{ij} - C_D \rho k^{\frac{3}{2}} / l \\ e_{ij} = \dfrac{\partial v_i}{\partial x_j} + \dfrac{\partial v_j}{\partial x_i} \\ G_\varepsilon = \dfrac{C_1 \varepsilon}{k} \mu_t e_{ij} \dfrac{\partial v_i}{\partial x_j} - C_2 \rho \varepsilon^2 / k \\ \mu_t = \rho C_\mu k^2 / \varepsilon \end{cases} \tag{13}$$

More detailed description of the variables can be found in reference (Ferziger and Peric 2002).

According to the basic thought of the Finite Volume Method (FVM), the integral of these conservation equations are carried out in computational grids of the air domain. Thus, the wind loads of steady analysis on the train are achieved.

2.2.2 ALE method for solving train–air dynamic boundary

When a train is running in crosswinds, the aerodynamic forces on the train are mainly determined by the flow structure around the train. Generally, the flow turbulence near the train is severer than that far from the train. A small perturbation of the car body will have influence on the flow structure nearby the train. For a long time, the train system and the train aerodynamic system are solved separately, which is not able to consider the coupling between the car body and the air. In the vehicle system dynamics (VSD), Lagrangian coordinates was usually used to describe the motion of the object. Eulerian coordinates was adopted in the computational fluid dynamics to study the state of the spot in space. As a result of the difference between the ways of motion description, it is difficult to carry out real-time co-simulation of train system and train aerodynamic system. In order to compromise the two descriptions and achieve the fluid-structure coupling analysis, ALE method is introduced.

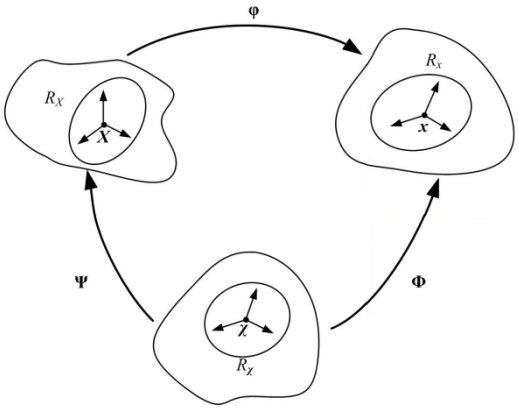

Fig. 4 Transformation of ALE configurations

In 1964, Noh (1964) put forward the ALE thought for the first time. The basic premise is that the mesh is neither stationary nor leeched onto the fluid particle, but can move in any arbitrary way in the system of coordinates. By this ALE method, it is easy to deal with mobile boundaries between the air and the train body.

There are three domains used in continuum mechanics: the material domain $\boldsymbol{R}_X$, the spatial domain $\boldsymbol{R}_x$ and the reference domain $\boldsymbol{R}_\chi$. The three domains and the one-to-one transformations relating the configurations are illustrated in Fig. 4. In the Lagrangian configuration $\boldsymbol{R}_X$, grid nodes of the air domain are permanently connected to the same associated air particles and thus the grid will follow the flow of air. In the Eulerian configuration $\boldsymbol{R}_x$, the grid nodes are immobile regardless of the flow of air. In the ALE configuration $\boldsymbol{R}_\chi$, the nodes of the computational mesh can be moved in arbitrarily velocity followed by the air. The ALE method combines the best features of both the Lagrangian and the Eulerian approaches. The mapping from the material domain $\boldsymbol{R}_X$ to the spatial domain $\boldsymbol{R}_x$ is represented by φ. The referential domain $\boldsymbol{R}_\chi$ is mapped into the material and spatial domains by Ψ and Φ respectively. The relation of these one-to-one transformations can be expressed as $\varphi=\Phi\cdot\Psi^{-1}$ (Donea *et al*. 2004).

In the Lagrangian configuration $\boldsymbol{R}_X$, the locomotion rule of air particle, $\boldsymbol{X}$, is depicted as

$$\boldsymbol{x} = \boldsymbol{x}(\boldsymbol{X}, t) \tag{14}$$

The motion rule of the node of the computational mesh is expressed as

$$\boldsymbol{x} = \boldsymbol{x}(\boldsymbol{\chi}, t) \tag{15}$$

The motion rule of the air particle, $\boldsymbol{X}$, in reference ALE configuration $\boldsymbol{R}_\chi$ is

$$\boldsymbol{\chi} = \boldsymbol{\chi}(\boldsymbol{X}, t) \tag{16}$$

The air particle velocity v_i in $\boldsymbol{R}_X$, the mesh velocity $\hat{v}_i$ in $\boldsymbol{R}_X$ and the air particle velocity w_i in $\boldsymbol{R}_\chi$ are expressed as

$$v_i = \left.\frac{\partial \boldsymbol{x}(\boldsymbol{X}, t)}{\partial t}\right|_{\boldsymbol{X}} \tag{17}$$

$$\hat{v}_i = \left.\frac{\partial \boldsymbol{x}(\boldsymbol{\chi}, t)}{\partial t}\right|_{\boldsymbol{\chi}} \tag{18}$$

$$w_i = \left.\frac{\partial \boldsymbol{\chi}(\boldsymbol{X}, t)}{\partial t}\right|_{\boldsymbol{X}} \tag{19}$$

The relation of velocities v_i, $\hat{v}_i$ and w_i is

$$c_i = v_i - \hat{v}_i = \frac{\partial \boldsymbol{x}(\boldsymbol{\chi}, t)}{\partial \chi_i} w_i \tag{20}$$

where c_i is the convective velocity, which denotes the relative velocity between the air and the mesh.

The time derivative of a physical quantity for a given air particle $\boldsymbol{X}$ is the local derivative plus a convective term, taking into account the relative motion between the material and reference

system.

$$\left.\frac{\partial f}{\partial t}\right|_{\boldsymbol{X}} = \left.\frac{\partial f}{\partial t}\right|_{\boldsymbol{\chi}} + \frac{\partial f}{\partial x_i} c_i \tag{21}$$

According to Reynolds transport theorem, the time derivative of the integral of a scalar function $f(\boldsymbol{x},t)$ over the time-varying arbitrary volume V_t can be expressed as

$$\left.\frac{\partial}{\partial t}\right|_{\boldsymbol{\chi}} \int_{V_t} f(\boldsymbol{x},t)\,\mathrm{d}V = \int_{V_t} \left.\frac{\partial f(\boldsymbol{x},t)}{\partial t}\right|_{\boldsymbol{x}} \mathrm{d}V + \int_{S_t} f(\boldsymbol{x},t)\hat{v}_i n_i\,\mathrm{d}S \tag{22}$$

in which the smooth function f is defined in the spatial domain. In Eq. (22) the volume V_t is bounded by a smooth closed surface S_t whose points at time t moving at a speed of the convective velocity $\hat{v}_i$; n_i is the unit vector outward normal to the surface S_t at time t. The first term on the right-hand side of the Eq. (22) is the spatial time derivative of the volume integral. The second term is the boundary integral, which represents the flux of the scalar quantity $f(\boldsymbol{x},t)$ across the fixed boundary of the volume V_t at time t.

After replacing the scalar function $f(\boldsymbol{x},t)$ in Eq. (22) by ρ, ρv_i, ρE, ρk and $\rho\varepsilon$ respectively and substituting the spatial time derivative $\partial f/\partial t$ as Eqs. (8)-(12), the right-hand side of the Eq. (22) can be transferred to the boundary integral based on the Gauss Law. Therefore, the ALE integral forms of Eqs. (8)-(12) can be written as

$$\int_V \frac{\partial \rho}{\partial t}\mathrm{d}V + \int_S \rho\left(v_j - \hat{v}_j\right) n_j \mathrm{d}S = 0 \tag{23}$$

$$\int_V \frac{\partial \rho v_i}{\partial t}\mathrm{d}V + \int_S \left(\rho u_i\left(v_j - \hat{v}_j\right) - p_{ij}\right) n_j \mathrm{d}S = \int_V \rho g_i \mathrm{d}V \tag{24}$$

$$\int_V \frac{\partial \rho E}{\partial t}\mathrm{d}V + \int_S \left(\rho E\left(v_j - \hat{v}_j\right) - p_{ij}v_i - \mu B\frac{\partial I}{\partial x_j}\right) n_j \mathrm{d}S = \int_V \rho v_j g_j \mathrm{d}V \tag{25}$$

$$\int_V \frac{\partial \rho k}{\partial \tau}\mathrm{d}V + \int_S \left(\rho k\left(v_j - \hat{v}_j\right) - \mu_{eff}\frac{\partial k}{\partial x_j}\right) n_j \mathrm{d}S = \int_V G_k \mathrm{d}V \tag{26}$$

$$\int_V \frac{\partial \rho \varepsilon}{\partial \tau}\mathrm{d}V + \int_S \left(\rho \varepsilon\left(v_j - \hat{v}_j\right) - \mu_{eff}\frac{\partial \varepsilon}{\partial x_j}\right) n_j \mathrm{d}S = \int_V G_\varepsilon \mathrm{d}V \tag{27}$$

In Eqs. (23)-(27), when $v_j = \hat{v}_j$, the ALE integral forms change to the Lagrangian forms. While $\hat{v}_j = 0$, they change to the Eulerian forms (Hirt *et al*. 1974).

As the ALE method allows flexible grids with air flowing, it avoids the problems of tracking interfaces in the Eulerian framework as well as large distortion encountered in the Lagrangian approach. Based on the FVM, the integral of all conservation equations will be conducted in time domain. Thus, the interaction between the train and the air can be numerically solved in the ALE reference coordinate.

As to the difference between the results of aerodynamic forces with and without considering the train–air interaction, a previous published paper by the authors (Yang *et al*. 2009) has reported

in the case of train speed of 160 km/h. When the train–air interaction is considered, the aerodynamic forces vary with the car body vibration. The maximum aerodynamic forces when considering the train–air interaction are usually larger than those not considering the coupling effect, in which the lift force, the lateral aerodynamic force and the overturning aerodynamic moment change only around 5%, whereas the yaw aerodynamic moment changes by approximately 25%. Although the differences are not too big, it will have some influence on the dynamic behavior of the train. And in some special cases, such as when two trains passing each other or the train running in a tunnel at high speed, the train-air dynamic interaction becomes very intense and cannot be ignored.

3. Procedure of numerical solution

For such a large dynamic system, numerical simulation is a key technique to obtain the detailed responses. In the ALE reference frame, the FVM is used to compute the air flow around the train in crosswinds. A program based on the vehicle–track coupled dynamics is developed to simulate the vehicle dynamical responses induced by the resulting aerodynamic loads and track irregularities. The dynamic boundary of the flow field caused by the vibration of the train is considered by use of the moving computation grid technique.

The solving process of air–train–track interaction system is shown in Fig. 5. The basic numerical solvers are composed of the solver for the train–track coupled system dynamics (TTSD), the solver for train aerodynamics (TAD) and the solver for moving grid of the flow field (MGF). In the vehicle–track coupled dynamics, as the wheel–rail contact frequency is up to 500 Hz and more, the stable time step must be very small. A new fast explicit integral method (Zhai method) (Zhai 1996) is adopted and the valid time step is 1.0×10^{-4} s. In the aerodynamics, however, such a small time step will result in very high computing cost, which is unacceptable for the numerical simulation. Numerical trial result shows that the calculation time step for the present aerodynamics could be set as 0.01s, which minimize the calculation time and ensure the numerical accuracy. In order to achieve the time synchronization, the solvers for TTSD, TAD and MGF communicate with each other by control commands. The communication of each solver is executed by the client-server mode, which is connected through the standard TCP/IP procotol. The main procedure is structured as follows:

(a) When the TAD server receives an action order from the MGF client, which means the updated grids (in the first step it is the primitive grid) are ready, it will read in the computational grids and let the TAD solver to calculate the aerodynamic loads of the train. After the TAD solution is accomplished, the TAD client will send an order to the TTSD server and provide the TTSD server with the wind loads.

(b) After receiving the order from the TAD client, the TTSD server will admit the wind loads and ask the TTSD solver to calculate the dynamic response of the train. Owning to the time step used in the TTSD solver is 1/100 of that in the TAD solver, the TTSD client would not send an order as well as the displacement of the train to the MGF server until the time stepping number of TTSD calculation reaches100.

(c) Once the MGF server gets the order from the TTSD client, it will accept the displacement of the train and ask the MGF solver to adjust the mesh of flow field according to the displacement of the train. Then the MGF client will send an order and the new grids to the TAD server.

So far, the fluid–structure coupling analysis in one time step has been finished. Step by step, the whole course of the air–train–track interaction can be numerically simulated. The running safety and the ride comfort of the train can then be evaluated. The detailed procedure for numerical simulation of the air–train–track interaction is illustrated in Fig. 6.

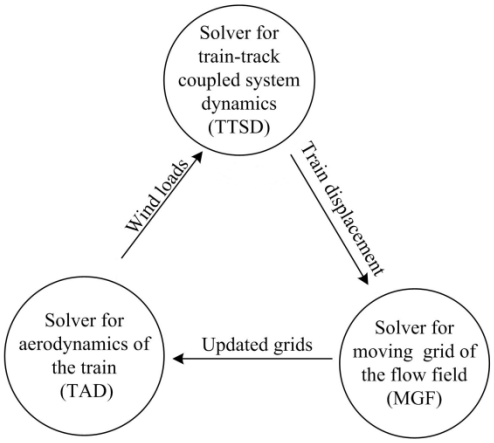

Fig. 5 Basic solution structure for air–train–track interaction

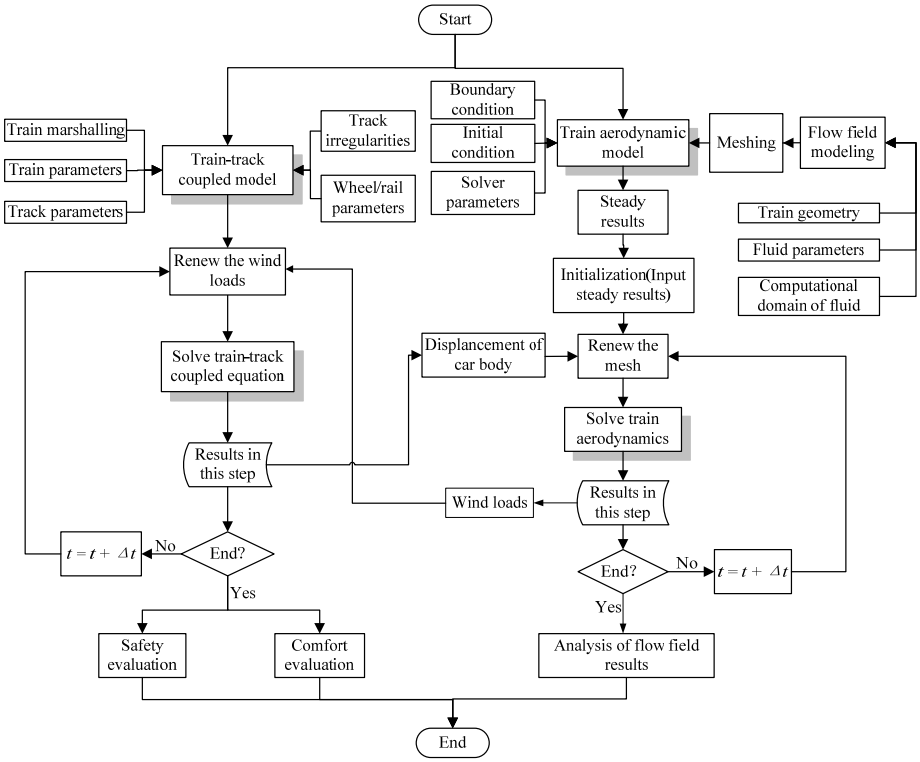

Fig. 6 Detailed procedure for numerical simulation of air–train–track interaction

4. Characteristics of flow structure around high-speed train

The flow structure around the high-speed train, which has great influence on the aerodynamic forces, can be displayed in the train–air interaction model. In order to investigate the dynamic behavior of high-speed train running on a straight embankment track substructure where crosswinds exist, a flow domain must first be set up. Fig. 7 illustrates the resultant wind speed V which depends on the natural wind speed W and the train speed U. β denotes the yaw angle of the resultant wind speed with respect to the train speed.

The computational resources of numerical simulation of a complete train with a length about 200 m are beyond those available on existing computers and hence only the flow fields of simplified train configurations can be reliably computed at present. According to the work by Cooper (1979), the certain distance of the flow structure downstream from the nose (less than one coach length) is more or less constant, which means a decrease in length does not alter the essential physical features of the flow as long as the total length remains above the limit suggested by Cooper. Therefore, the length of the train is limited to that of a Chinese Electric Multiple Unit (EMU) train assembly consisting of a head car, a middle car and a tail car, as shown in Fig. 8. The total length of the train is 75 m with a length to width to height ratio of 1:0.0451:0.0493. In addition, the train geometry is further simplified for the computations by neglecting surface and underside details such as mirrors, windshield wipers and mechanical parts. Also, the inter-carriage gap is neglected and the track and wheelsets are not included in the train–air interaction model.

The flow around the train remains different to that past aero and space vehicles because the interaction between the underside flow and the ground cannot be ignored. Owing to the geometrical characteristics and operational speeds of trains, the resulting flow field is essentially a three-dimensional turbulent one. In general, the associated variations in density are negligible and the flow is treated as incompressible.

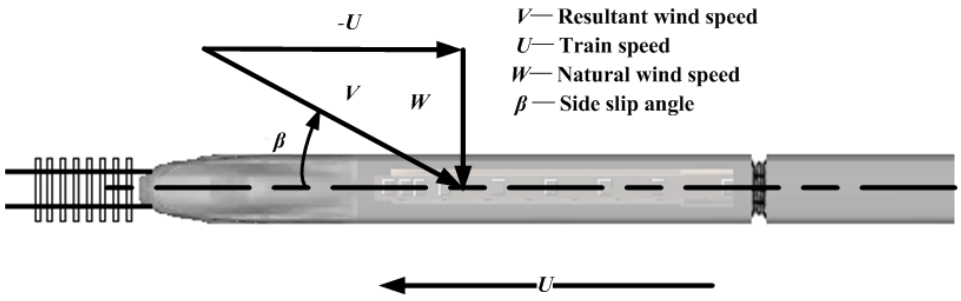

Fig. 7 Illustration of train speed and wind speed

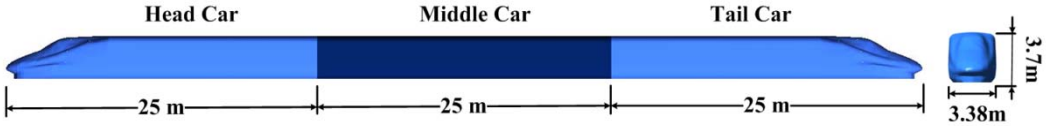

Fig. 8 Train geometry model

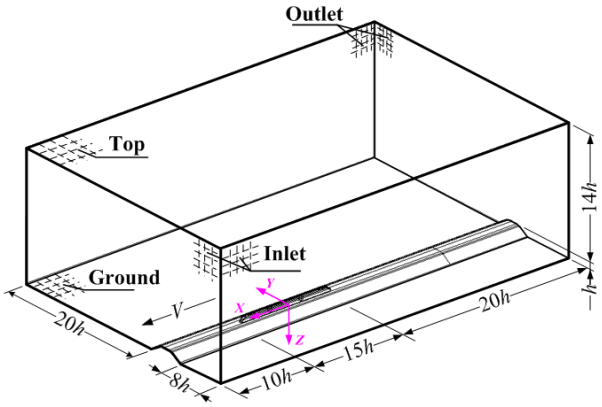

Fig. 9 Computational domain of fluid

Fig. 9 shows the dimensions of the flow domain used in calculation. In order to minimize the boundary effect, the calculation domain should be large enough. In the calculation, the length and height of the flow domain are 45*h* and 15*h*, where *h* is the height of the embankment (*h*=5 m) that is chosen as the characteristic length. In consideration of the difference between the upstream and downstream flow structures, the width of the downstream domain is larger than that of the upstream domain, as shown in Fig. 9. The coordinate system is located at the centroid of the middle car. At the inlet, the steady mean resultant wind enters the flow domain with the turbulence intensity of 5% and the length scale of 0.4 m. On the outlet and top, the entrainment boundary is adopted and the relative pressure is set as 0 Pa. On the ground and solid surfaces, the standard wall functions for smooth walls were applied to simplify the calculation. The roughness of the ground boundary should be considered for more precise computation. The train is stationary in the flow field, whereas the track, embankment and ground move at the speed equal and opposite to the real train speed.

For the numerical predictions, the computational domain of fluid is resolved by an unstructured grid. From Figs. 10 and 11, it can be seen that surface grids are generated on the car surface. The total grid number is 2.5×10^6 control volumes. A commercial grid generation package ICEM CFD is utilized to generate the grid.

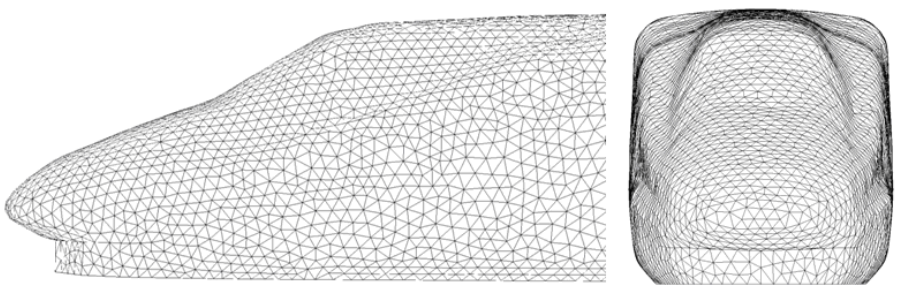

Fig. 10 Surface grids of train model

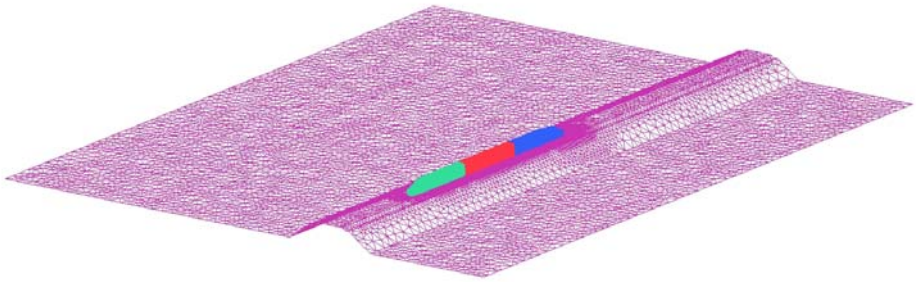

Fig. 11 Surface mesh of the embankment model

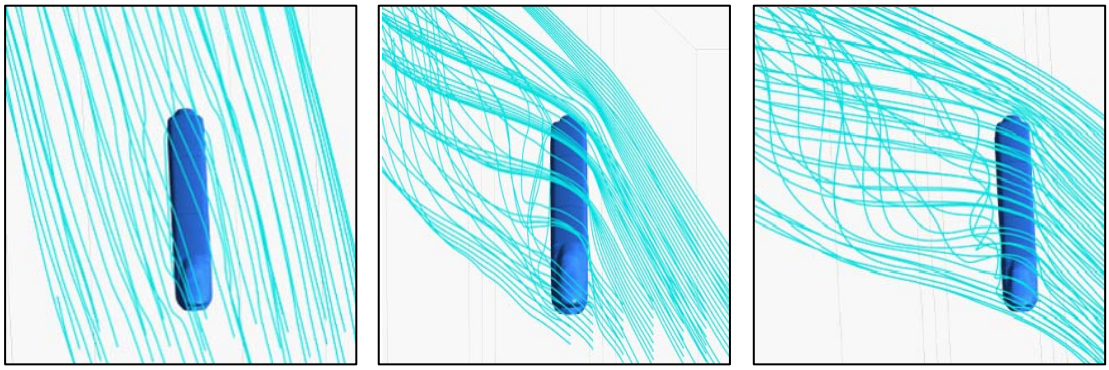

(a) β=2.58° (b) β=10.31° (c) β=25.78°

Fig. 12 Schematic view of flow structures around high-speed train

The flow structure around the wall is mainly determined by the Reynolds number and the yaw angle. With low Reynolds number, the flow attached to the train body maintains being laminar. As the Reynolds number increases, the flow begins to detach from the car body. When it reaches some critical value, the yaw angle starts to play a dominant role on the flow structure around the train. Fig. 12 depict the 3-D streamline distributions of the flow structure at one step of the whole course of air–train–track interaction for yaw angles of 2.58° (train speed 400 km/h and wind speed 5 m/s), 10.31° (train speed 300 km/h and wind speed 15 m/s) and 25.78° (train speed 200 km/h and wind speed 25 m/s), respectively. The 2-D streamlines of the three cases at different locations on the X-axis are sketched in Fig. 13.

As shown in Fig. 12(a), when the yaw angle is simply small β=2.58°, the boundary layer basically in a laminar state reveals no obvious separation from the surface of the train, whereas its thickness increases along the travel direction from the front to the rear. When the flow evolves downstream, as seen in Fig. 13(a), the flow across the bottom of the head car separates and results in the generation of a minor lee-vortex at x/h=4, namely the middle cross-section of the head car. The vortex grows steadily along the negative X-axial direction and keeps moving upwards and outwards. At the rear end of tail car where x/h=-7.2, it is observed to be convected by the flow away from the train.

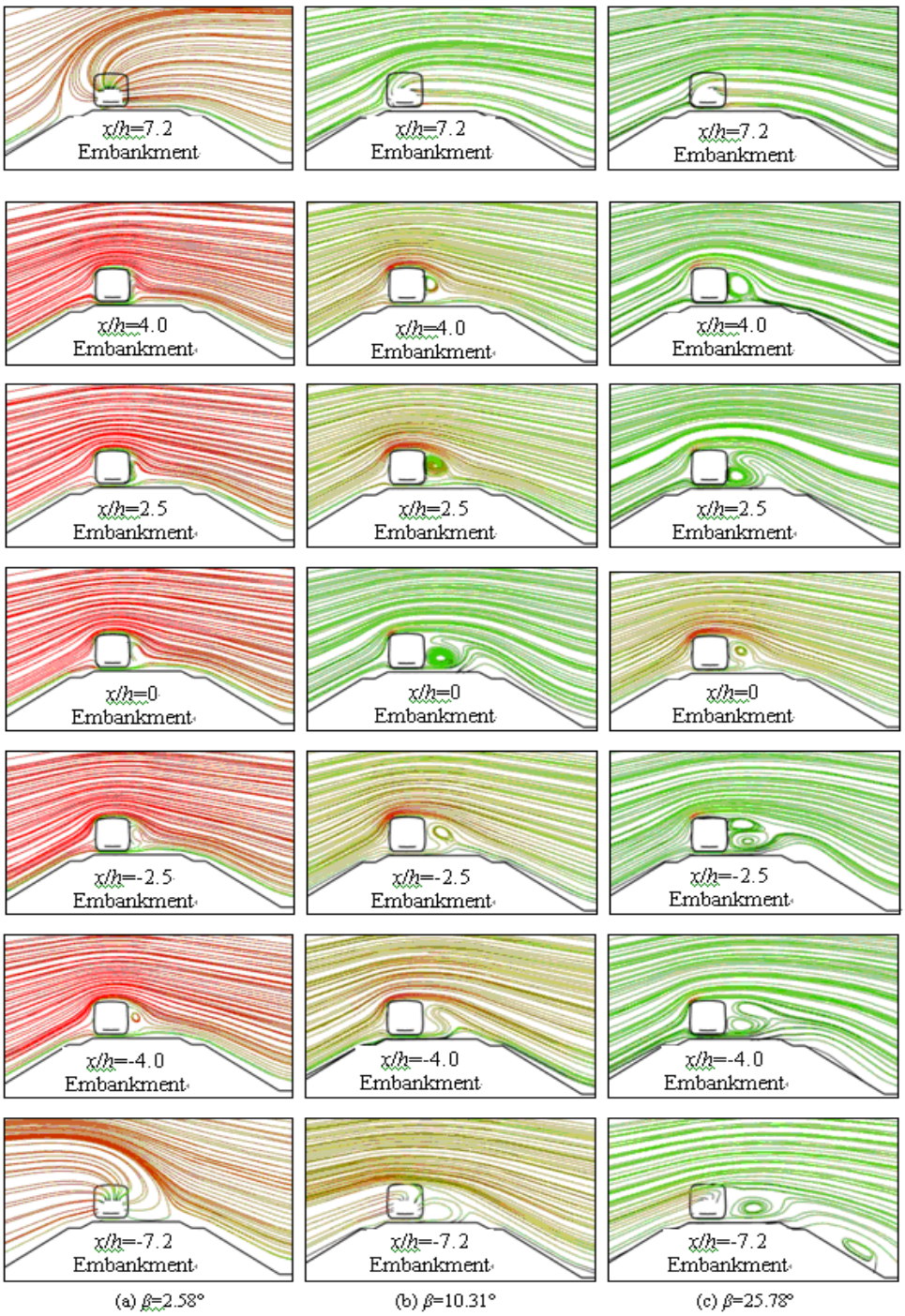

Fig. 13 2-D streamlines for different locations on the X-axis

With the increase of the yaw angle, for the β=10.31° case, as seen in Fig. 12(b), the flow turbulence becomes severe and the flow detaches earlier. As a result, a greater vortex is shed from the lower leeward side of the head car where x/h=4, as seen in Fig. 13(b). When the vortex moves downstream, it is constantly intensified and reaches the maximum at x/h=0. After that, it gradually decays and transports away from the train.

The case for yaw angle β=25.78° is illustrated in Fig. 12(c). The turbulent flow becomes more visible and a clear separation over the leading nose is observed. As the flow moves downstream to the rear of the head car where x/h=2.5, the vortex originating from the nose totally separates from the surface of the train. Simultaneously, another vortex is shed from the bottom of the car. Afterward, as shown in Fig. 13(c) for x/h=0.0 and x/h=-2.5, the nose vortex gradually moves downward and outward under the action of the roof flow, accompanied by a weakened intensity. In contrast, the lower vortex continually moves upward and grows. Owing to the fading of the nose vortex and the enhancement of the lower vortex, another new separate vortex is generated by the flow over the leading edge of the roof, as depicted in Fig. 13(c) for x/h=-2.5 and x/h=-4. This vortex interacts strongly with the lower vortex at the bottom and results in a powerful vortex which will be further strengthened when encountering the roof flow of the tail car.

In all cases aforementioned, with the increase of the yaw angle, the flow turbulence surrounding the car becomes more and more severe. It is deduced that the yaw angle plays a key role in flow structure.

5. Analysis of high-speed train running safety in crosswinds

The crosswind has great influence on dynamic behavior of a train running on a track, especially in high-speed operation. In this section, numerical simulation will be carried out with the method described above for a high-speed EMU train running on a ballasted track in crosswinds. In calculation, the crosswind speed varies in range from 5 m/s to 30 m/s. The excitation of track geometry irregularity is also considered. In the calculation, the German high-speed track spectrum is adopted. The main parameters of the EMU and the track used are given in Tables 1 and 2, respectively.

When a train is running on the track, a priority must be given to the running safety, especially in crosswind environment. There are four indices commonly used as safety criteria in vehicle system dynamics (Garg and Dukkipati 1984), i.e., the derailment coefficient, the wheel-load reduction ratio, the overturning coefficient and the wheel–rail lateral force. Traditionally, when considering the crosswind conditions, much attention was paid to the overturning coefficient. But this is not enough for guaranteeing the running safety of a train. Other safety accidents, such as the train derailment, may happen before the train is overturned. In order to ensure the running safety of high-speed train on elastic track under crosswinds, the four safety indices are all investigated in the paper rather than only considering the overturning coefficient.

5.1 Derailment coefficient

In the vehicle dynamics, the derailment coefficient (Nadal 1908) is often adopted to estimate the possibility of vehicle derailing. According to the specifications for running safety of railway vehicles used in Chinese Railways, the limit of derailment coefficient is 0.8 for high-speed trains. Fig. 14 compares the maximum derailment coefficients of the three cars at different crosswind

speeds, under the train speed of 300 km/h. As seen from Fig. 14, the derailment coefficient of the head car increases rapidly with the increasing crosswind speed. It indicates that the head car is much more dangerous than other cars.

Table 1 Main parameters of the EMU

Notation	Parameter	Value	Unit
M_c	Car body mass	39600	kg
M_t	Bogie mass	3200	kg
M_w	Wheelset mass	2000	kg
I_{cx}	Mass moment of inertia of car body about X axis	128304	kg m^2
I_{cy}	Mass moment of inertia of car body about Y axis	1940400	kg m^2
I_{cz}	Mass moment of inertia of car body about Z axis	1673100	kg m^2
I_{tx}	Mass moment of inertia of bogie about X axis	2592	kg m^2
I_{ty}	Mass moment of inertia of bogie about Y axis	1752	kg m^2
I_{tz}	Mass moment of inertia of bogie about Z axis	3200	kg m^2
I_{wx}	Mass moment of inertia of wheelset about X axis	720	kg m^2
I_{wy}	Mass moment of inertia of wheelset about Y axis	84	kg m2
I_{wz}	Mass moment of inertia of wheelset about Z axis	980	kg m^2
K_{px}	Stiffness coefficient of primary suspension along X axis	10.68	MN m^{-1}
K_{py}	Stiffness coefficient of primary suspension along Y axis	7.48	MN m^{-1}
K_{pz}	Stiffness coefficient of primary suspension along Z axis	1.176	MN m^{-1}
K_{sx}	Stiffness coefficient of secondary suspension along X axis	0.1891	MN m^{-1}
K_{sy}	Stiffness coefficient of secondary suspension along Y axis	0.1891	MN m^{-1}
K_{sz}	Stiffness coefficient of secondary suspension along Z axis	0.2205	MN m^{-1}
C_{pz}	Damping coefficient of primary suspension along Z axis	19.6	kN s m^{-1}
C_{sy}	Damping coefficient of secondary suspension along Y axis	9.0	kN s m^{-1}
C_{sz}	Damping coefficient of secondary suspension along Z axis	10.0	kN s m^{-1}
l_c	Semi-longitudinal distance between bogies	8.6875	m
l_t	Semi-longitudinal distance between wheelsets in bogie	1.25	m
R_0	Wheel radius	0.43	m

Table 2 Main parameters of the ballasted track

Notation	Parameter	Value (per rail seat)	Unit
E	Elastic modulus of rail	2.059×10^{11}	N m^{-2}
ρ	Density of rail	7.86×10^{3}	kg m^{-3}
I_0	Torsional inertia of rail	3.741×10^{-5}	m^4
I_y	Rail second moment of area about Y axis	3.217×10^{-5}	m^4
I_z	Rail second moment of area about Z axis	5.24×10^{-6}	m^4
GK	Rail torsional stiffness	1.9587×10^{5}	N m rad^{-1}
m_r	Rail mass per unit length	60.64	kg m^{-1}
M_s	Sleeper mass (half)	125.5	kg
K_{pv}	Fastener stiffness in vertical direction	6.5×10^{7}	N m^{-1}
K_{ph}	Fastener stiffness in lateral direction	2.0×10^{7}	N m^{-1}
C_{pv}	Fastener damping in vertical direction	7.5×10^{4}	N s m^{-1}
C_{ph}	Fastener damping in lateral direction	5.0×10^{4}	N s m^{-1}
K_{bv}	Ballast stiffness in vertical direction	8.0×10^{7}	N m^{-1}
K_{bh}	Ballast stiffness in lateral direction	5.0×10^{7}	N m^{-1}
C_{bv}	Ballast damping in vertical direction	5.88×10^{4}	N s m^{-1}
C_{bh}	Ballast damping in lateral direction	1.0×10^{5}	N s m^{-1}
K_w	Ballast shear stiffness	7.84×10^{7}	N m^{-1}
C_w	Ballast shear damping	8.0×10^{4}	N s m^{-1}
K_{fv}	Subgrade stiffness	6.5×10^{7}	N m^{-1}
C_{fv}	Subgrade damping	3.115×10^{4}	N s m^{-1}

When the wind force is acting on the car body, the dynamic performances of the wheels on the windward side and the leeward side are different. The comparisons of the derailment coefficients between the windward side and the leeward side are carried out in Figs. 15(a)-15(c) for the head, middle and tail cars, respectively. All the graphs show that the derailment coefficients on the leeward side are larger than those on the windward side in crosswinds. Particularly, for the head car, the difference between the windward side and the leeward side is pronounced at the crosswind speed above 15 m/s.

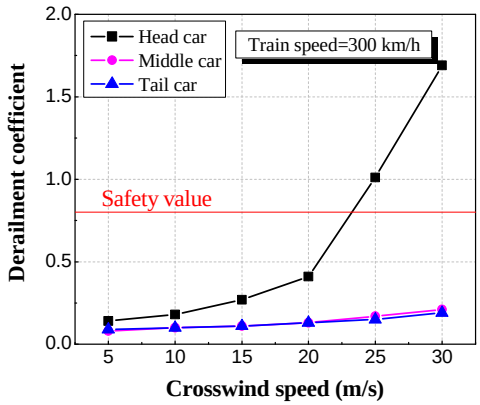

Fig. 14 Derailment coefficients at different crosswind speeds

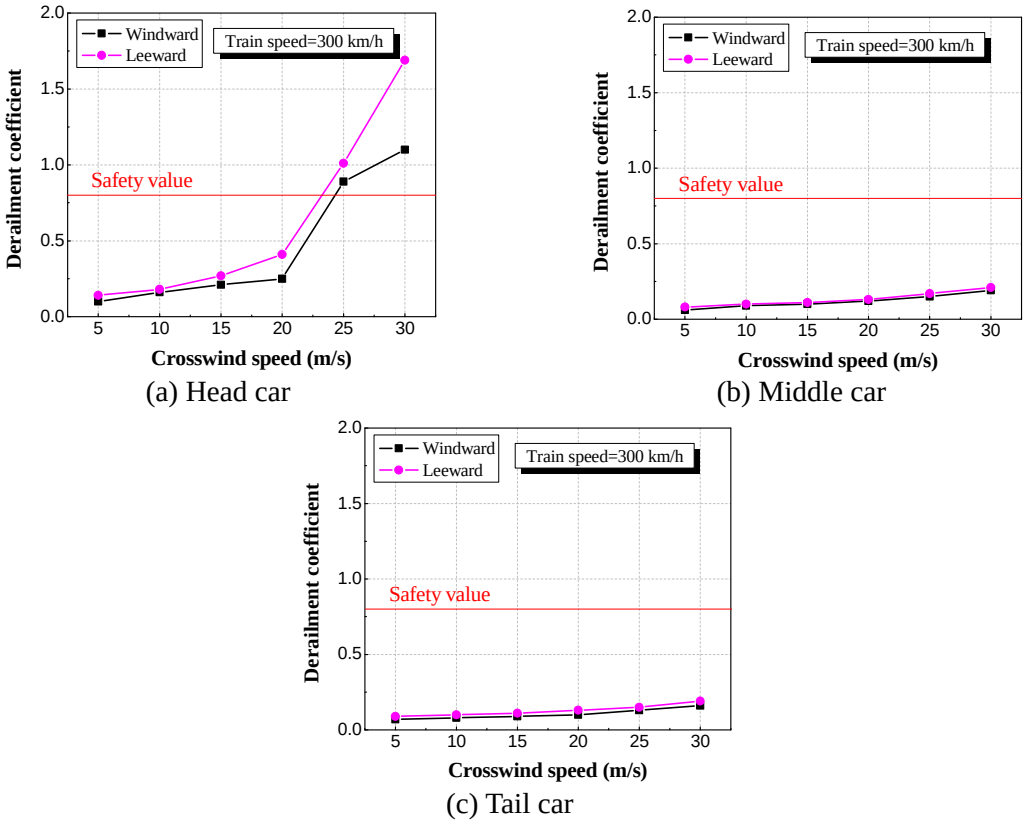

Fig. 15 Derailment coefficients on windward and leeward sides

5.2 Wheel-load reduction ratio

The wheel-load reduction ratio is another important indices used for estimating the running safety of the train. If the wheel-load of the train is greatly reduced, the operational safety of high-speed train will be seriously threatened. The threshold of dynamical wheel-load reduction ratio is set as 0.9 for some evaluation tests of train dynamic performance in China (Zhai 2015). Fig. 16 sketches the maximum reduction ratios of wheel-load at different crosswind speeds, with the train speed of 300 km/h. It is seen that, with the increase of crosswind speed, the wheel-load reduction ratio rises most quickly for the head car, followed by the middle car. As for the tail car, it is almost unchanged as result of the small change of lateral aerodynamic forces and overturning moments. That is to say, the head car will firstly cross over the safety threshold which means its security is the lowest.

5.3 Overturning coefficient

While evaluating the train stability in crosswinds, overturning coefficient is commonly used. When the overturning coefficient is above 0.8, the running train is considered as dangerous in Chinese Railways. The maximum overturning coefficients at different crosswind speeds and different train speeds are described in Figs. 17 and 18, respectively. Notice that the tail car may be overturned in the opposite direction of the head car and the middle car. Thus, negative numbers are utilized to illustrate the tail car case. It is shown that, with the increase of crosswind speed or train speed, the absolute values of overturning coefficients in all cases will increase. The aerodynamic performance of the head car is the worst, followed by the tail car and the middle car.

5.4 Wheel–rail lateral force

In order to prevent the damage of track structure, the wheel–rail lateral force is usually not allowed to exceed 0.4 times of the static axle load. For the train used in this study, the threshold of the wheel–rail lateral force is 53 kN. In Fig. 19, the maximum wheel–rail lateral forces on the three cars at different crosswind speeds are compared, with the train speed of 300 km/h. There is no evident discrepancy in all cases at low crosswind speeds. With the increase of the wind speed, the wheel–rail lateral forces in all cases rise more or less, where the growth of the head car is much faster than the other two. For example, when the crosswinds speed reaches 30 m/s, the wheel–rail lateral force of the head car is 158.96 kN, far beyond the safety threshold, whereas those of the other cars are below 20 kN. This result further verifies that the head car has the lowest security.

5.5 Critical wind speed

From aforementioned results, it could be concluded that the head car is the most dangerous among the three cars, no matter which dynamic index is chosen as the safety criterion. Consequently, the running safety of high-speed train on track depends mainly on the head car in crosswinds. Therefore, the method to determine the critical wind speed is discussed below according to the safety indices of the head car.

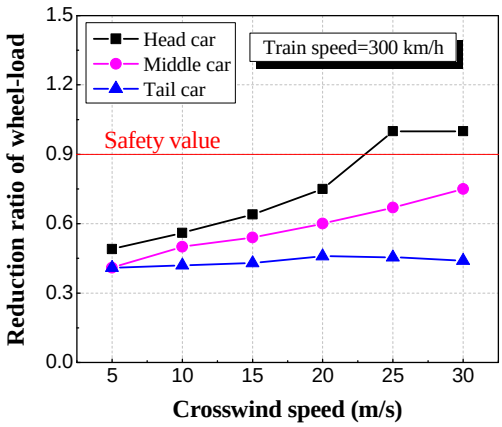

Fig. 16 Wheel-load reduction ratios at different crosswind speeds

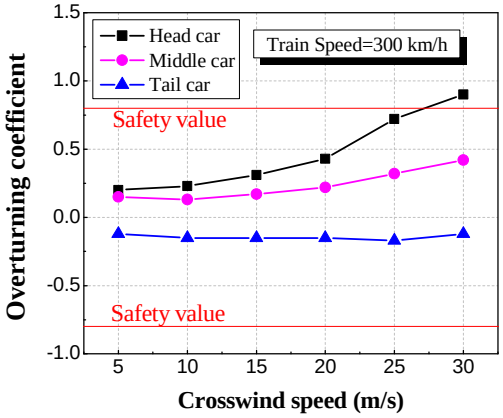

Fig. 17 Overturning coefficients vs. crosswind speeds at train speed 300 km/h

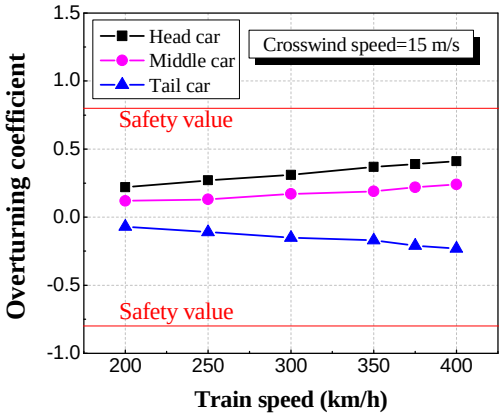

Fig. 18 Overturning coefficients vs. train speeds at wind speed 15 m/s

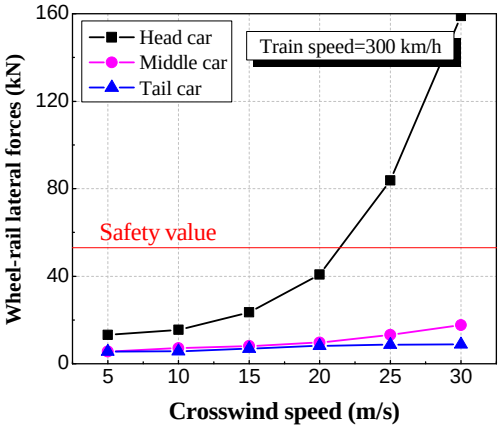

Fig. 19 Wheel–rail lateral forces at different crosswind speeds

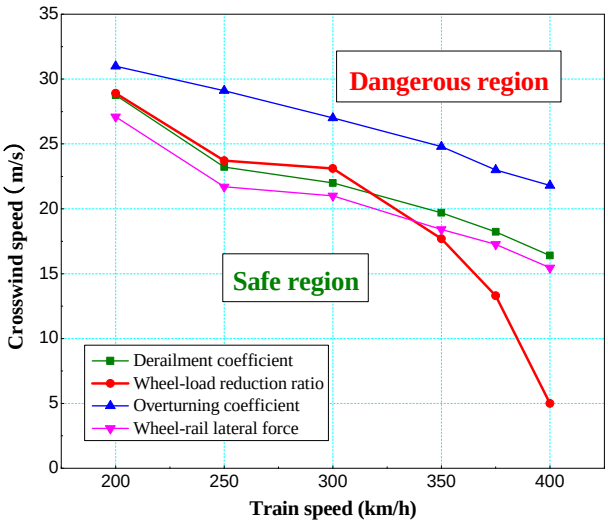

Fig. 20 Critical wind speeds vs. train speeds from 200 to 400 km/h

Through numerical computation for different wind speeds and for different train speeds, the critical wind curves judged by different safety indices can be determined with the similar method used by Jin *et al.* (2013) and Guo *et al.* (2013), as shown in Fig. 20. Here the train speed varies from 200 km/h to 400 km/h. It can be obviously seen from Fig. 20 that the critical wind speed gradually declines with the increase of the train speed. When the overturning coefficient of head car reaches its limit, the other three indices, namely the derailment coefficient, the wheel-load reduction ratio and the wheel–rail lateral force, have already exceeded their safety values. Therefore, it is convinced that the traditional assessment of critical wind speed judged by the overturning coefficient overestimates the running safety of the train on the track. Through more

careful observation, it can be found that the critical wind speeds judged by the derailment coefficient, the wheel-load reduction ratio and the wheel–rail lateral force show no evident discrepancy with the train speed between 200 km/h and 300 km/h, in which the wheel–rail lateral force gives the lowest wind speed. When the train speed exceeds 300 km/h, however, the wheel-load reduction ratio begins to play a dominated role on the safety evaluation; although, it seems over-conservative to estimate the critical wind speed. That is because the wheel-load reduction ratio not only depends on the crosswind, but also considerably relates to the shortwave track irregularity. When the train speed is very high, shortwave irregularity seriously impairs the running safety.

In order to guarantee the running safety of high-speed trains running on elastic track in crosswind circumstances, all the dynamic safety indices of train must be below their thresholds. From the results shown in Fig. 20, the wheel-load reduction ratio and the wheel–rail lateral force are recommended as the dominant safety indices for estimating the critical wind speed.

6. Conclusions

An air–train–track interaction model has been set up in this paper for investigating the overall dynamics of the vehicle–track coupled system in crosswinds, composed of a train–track interaction model and a train–air interaction model. The train–track interaction model is established on the basis of the theory of vehicle–track coupled dynamics. The train–air interaction model is built by the finite volume method based on Navier–Stokes equation and k-ε two equation turbulence model, in which the ALE method is employed to deal with the dynamic boundary between the train and the air. The running safety of a high-speed train on an elastic track in crosswinds has been evaluated under the presented framework.

On the basis of the analysis and discussion of numerical results, it can be concluded that:

(a) The yaw angle has great influence on the flow structure around the train in crosswinds.

(b) The dynamic indices of the head car are much larger than those of other cars in crosswinds. It indicates that the head car is much more dangerous than other cars.

(c) The traditional method for assessment of the critical wind speed using the overturning coefficient will overestimate the running safety of the train on the elastic track in crosswinds.

(d) In order to guarantee the safety of high-speed trains running on tracks in crosswinds, the wheel-load reduction ratio and the lateral wheel–rail force are recommended as the dominant safety assessment indices to estimate the critical wind speed.

It is worth mentioning that, some characters involved in the complex air–train–track interaction system have been simplified in this paper, e.g. details of car geometry feature, the effect of ground boundary layer, etc. There are many works need to be done in the future.

Acknowledgements

This work was supported by the National Key Basic Research Program of China (973 Program) under grant numbers 2013CB036206 and 2007CB714706, and by the National Natural Science Foundation of China (NSFC) under grants U1234209.

References

Baker, C.J. (1991a), "Ground vehicles in high cross wind, Part I: steady aerodynamic forces", *J. Fluid. Struct.*, **5**(1), 69-90.

Baker, C.J. (1991b), "Ground vehicles in high cross wind, Part II: unsteady aerodynamic forces", *J. Fluid. Struct.*, **5**(1), 91-111.

Balzer, Z.A. (1977), "Atmospheric turbulence encountered by high-speed ground transport vehicles", *J. Mech. Eng. Sci.*, **19**(5), 227-235.

Cheli, F., Ripamonti, F., Rocchi, D. and Tomasini, G. (2010), "Aerodynamic behaviour investigation of the new EMUV250 train to cross wind", *J. Wind Eng. Ind. Aerod.*, **98**(4-5), 189-201.

Chiu, T.W. (1991), "A two-dimensional second-order vortex panel method for the flow in a crosswind over a train and other two-dimensional bluff bodies", *J. Wind Eng. Ind. Aerod.*, **37**(1), 43-64.

Chiu, T.W. (1995), "Prediction of the aerodynamic loads on a railway train in a crosswind at large yaw angles using an integrated two- and three-dimensional source/vortex panel method", *J. Wind Eng. Ind. Aerod.*, **57**(1), 19-39.

Cooper, R.K. (1979), "The effect of crosswinds on trains", *Proceedings of the ASME–CSME Conference on Aerodynamics of Transportation, Niagara*, June 18-20.

Cooper, R.K. (1984), "Atmospheric turbulence with respect to moving ground vehicles", *J. Wind Eng. Ind. Aerod.*, **17**(2), 215-238.

Dahlberg, T. (1995), "Vertical dynamic train/track interaction - verifying a theoretical model by full-scale experiments", *Vehicle Syst. Dyn.*, **24**(1), 45-57.

Diedrichs, B. (2003), "On computational fluid dynamics modeling of crosswind effects for high-speed rolling stock", *J. Rail Rapid Transit*, **217** (3), 203-226.

Diedrichs, B., Sima, M., Orellano, A. and Tengstrand, H. (2007), "Crosswind stability of a high-speed train on a high embankment", *J. Rail Rapid Transit*, **221**(2), 205-225.

Diedrichs, B. (2010), "Aerodynamic crosswind stability of a regional train model", *Proceedings of the Institution of Mechanical Engineers, Part F: J. Rail Rapid Transit*, **224**(6), 580-591.

Donea, J., Huerta, A., Ponthot, J.-Ph. and Rodríguez-Ferran, A. (2004), "Arbitrary Lagrangian–Eulerian Methods", *Encyclopedia of Computational Mechanics*, **1**, Fundamentals.

Ferziger, J.H. and Peric, M. (2002), *Computational Methods for Fluid Dynamics*, Springer-Verlag.

Garg, V.K. and Dukkipati, R.V. (1984), *Dynamics of Railway Vehicle Systems*, *Canada: Academic Press*.

Guo, W.W., Xia, H. and Zhang, N. (2013), "Dynamic responses of Tsing Ma Bridge and running safety of trains subjected to Typhoon York", *Int. J. Rail Transportation*, **1**(3), 181-192.

Herbsta A.H., Mulda T.W. and Efraimsson G. (2014), "Aerodynamic prediction tools for high-speed trains", *Int. J. Rail Transportation*, **2**(1), 50-58.

Hirt, C.W., Amsden, A.A. and Cook, J.L. (1974), "An arbitrary Lagrangian–Eulerian computing method for all flow speeds", *J. Comput. Physics*, **14**(3), 227-253.

Jin, X.S., Xiao, X.B., Ling, L., Zhou, L. and Xiong, J.Y. (2013), "Study on safety boundary for high-speed train running in severe environments", *Int. J. Rail Transportation*, **1**(1-2), 87-108.

Khier, W. and Le Devehat, E. (1997), *CFD Methodology*, TRANSAERO (Transient Aerodynamics for Railway System Optimisation) WP1 Technical Report, Report Ref. 1M7S23T1.DA.

Khier, W., Breuer, M. and Durst, F. (2000), "Flow structure around trains under side wind conditions: a numerical study", *Comput. Fluids*, **29**(2), 179-195.

Khier, W., Breuer ,M. and Durst, F. (2002), "Numerical computation of 3-D turbulent flow around high-speed trains under side wind conditions", *TRANSAERO — A European Initiative on Transient Aerodynamics for Railway System Optimisation Notes on Numerical Fluid Mechanics and Multidisciplinary Design (NNFM)*, Springer-Verlag.

Li, Y.F. and Tian, H.Q. (2012), "Lateral aerodynamic performance and speed limits of double-deck container vehicles with different structures", *J. Central South Univ.*, **19**(7), 2061-2066.

Li, Y.L., Qiang, S.Z., Liao, H.L. and Xu, Y.L. (2005), "Dynamics of wind-rail vehicle-bridge systems", *J.*

Wind Eng. Ind. Aerod., **93**(6), 483-507.
Li, Y.L., Hu, P., Xu, Y.L., Zhang, M.J. and Liao, H.L. (2014), "Wind loads on a moving vehicle–bridge deck system by wind-tunnel model test", *Wind Struct.*, **19**(2), 145-167.
Li, Y.L., Xiang, H.Y., Wang, B., Xu, Y.L. and Qiang, S.Z. (2013), "Dynamic analysis of wind-vehicle-bridge system with two trains interaction", *Adv. Struct. Eng.*, **16**(10), 1663-1670.
Nadal, M. J. (1908), "Locomotives a vapeur, collection encyclopedie scientifique", *Biblioteque de Mecanique Appliquee et Genie*, **186**, 56-67.
Noh, W.F. (1964), "CEL: A time-dependent two-space dimensional coupled Eulerian–Lagrangian code", *Methods Comput. Physics*, **3**, 123-144.
Rezvani, M.A. and Mohebbi, M. (2014), "Numerical calculations of aerodynamic performance for ATM train at crosswind conditions", *Wind Struct.*, **18**(5), 529-548.
Sterling, M., Quinn, A.D. and Hargreaves, D.M., Chelic, F., Sabbionic, E, Tomasinic, G., Delaunayd, D., Bakera, C.J. and Morvane, H. (2010), "A comparison of different methods to evaluate the wind induced forces on a high sided lorry", *J. Wind Eng. Ind. Aerod.*, **98**(1), 10-20.
Sun, Y.Q. and Dhanasekar, M. (2002), "A dynamic model for the vertical interaction of the rail track and wagon system", *Int. J. Solids Struct.*, **39**(5), 1337-1359.
Suzuki, M., Nakade, K. and Fujimoto, H. (2001), "Study on interaction between vehicle dynamics and aerodynamic force on high speed train in tunnel", *RTRI Report.*, **15**(5), 19-24.
Xia, H., Guo, W.W., Zhang, N. and Sun, G.J. (2008), "Dynamic analysis of a train–bridge system under wind action", *Comput. Struct.*, **86**(19-20), 1845-1855.
Xu, Y.L. and Ding, Q.S. (2006), "Interaction of railway vehicles with track in crosswinds", *J. Fluid. Struct.*, **22**(3), 295-314.
Xu, Y. L. (2013), *Wind effects on cable-supported bridges*, Singapore, John Wiley & Sons.
Yang, J.Z., Bi, H.Q. and Zhai, W.M. (2009), "Dynamic analysis of train in cross-winds with the Arbitrary Lagrangian–Eulerian method", *J. China Railway Soc.*, **31**(2), 120-124 (In Chinese).
Zhai, W.M. (1996), "Two simple fast integration methods for large-scale dynamic problems in engineering", *Int. J. Numer. Meth. Eng.*, **39**(24), 4199-4214.
Zhai, W.M. (2015), *Vehicle-Track Coupled Dynamics*, 4th Ed., Beijing: Science Press (In Chinese).
Zhai, W.M., Cai, C.B. and Guo, S.Z. (1996), "Coupling model of vertical and lateral vehicle/track interactions", *Vehicle Syst. Dyn.*, **26**(1), 61-79.
Zhai, W.M. and Wang, K.Y. (2006), "Lateral interactions of trains and tracks on small-radius curves: simulation and experiment", *Vehicle Syst. Dyn.*, **44**(Supplement 1), 520-530.
Zhai, W.M. and Wang, K.Y. (2010), "Lateral hunting stability of railway vehicles running on elastic track structures", *J. Comput. Nonlinear Dyn. - ASME*, **5**(4), 041009-1–9.
Zhai, W.M., Wang, K.Y. and Cai, C.B. (2009), "Fundamentals of vehicle–track coupled dynamics", *Vehicle Syst. Dyn.*, **47**(11), 1349-1376.
Zhai, W.M. and Sun, X. (1994), "A detailed model for investigating vertical interaction between railway vehicle and track", *Vehicle Syst. Dyn.*, **23**(Supplement 1), 603-615.